AGU PUBLICATIONS

JGR

Journal of Geophysical Research: Atmospheres

RESEARCH ARTICLE
10.1002/2013JD021195

Key Points:
- Svalbard airglow temperatures are adjusted for seasonal and solar variations
- The solar response coefficient is 3.6 K/100 SFU with an uncertainty of 4.0 K
- The long-term mesospheric temperature trend is a near-zero trend

Correspondence to:
S. E. Holmen,
siljeh@unis.no

Citation:
Holmen, S. E., M. E. Dyrland, and F. Sigernes (2014), Long-term trends and the effect of solar cycle variations on mesospheric winter temperatures over Longyearbyen, Svalbard (78°N), *J. Geophys. Res. Atmos.*, *119*, 6596–6608, doi:10.1002/2013JD021195.

Received 13 NOV 2013
Accepted 23 MAY 2014
Accepted article online 27 MAY 2014
Published online 13 JUN 2014

Long-term trends and the effect of solar cycle variations on mesospheric winter temperatures over Longyearbyen, Svalbard (78°N)

Silje E. Holmen[1,2,3], Margit E. Dyrland[1,2], and Fred Sigernes[1,2]

[1]University Centre in Svalbard, Longyearbyen, Norway, [2]Birkeland Centre for Space Science, Bergen, Norway, [3]UiT—Arctic University of Norway, Tromsø Geophysical Observatory, Tromsø, Norway

Abstract This paper gives an update on the long-term trend in hydroxyl (OH*) airglow winter temperatures measured by a 1 m Ebert-Fastie spectrometer in Longyearbyen, Svalbard (78°N, 16°E), from 1983 to 2013. The temperatures are derived through synthetic fits of measured airglow spectra of the OH*(6-2) vibrational state. The data set is corrected for seasonal variations by subtracting the mean climatology. Also, solar cycle dependence is investigated. A solar response coefficient of 3.6 K ± 4.0 K/100 solar flux units (SFU) is calculated from F10.7 cm solar radio flux data. After subtraction of the climatology and solar response, the remaining long-term trend is a near-zero trend, −0.2 K ± 0.5 K/decade. Trend analysis of monthly temperatures indicates positive trends for November, January, and February and a negative trend for December, but the uncertainties are high.

1. Introduction

For many years, great attention has been given to the ongoing change in the Earth's climate. Most studies have focused on the climate change in the lower atmosphere [e.g., *Dickinson and Cicerone*, 1986; *Brasseur and Hitchman*, 1988], but during the last decades attention regarding climate change issues has also been drawn toward the middle and upper atmosphere. Model studies report that global warming at the Earth's surface has its counterpart in cooling of the stratosphere and mesosphere due to global increase of CO_2 and other greenhouse gases [*Akmaev and Fomichev*, 1998, 2000]. In this part of the atmosphere, greenhouse gases absorb energy and radiate it back to space, which leads to cooling. Some studies indicate that temperature change takes place first in the mesosphere and lower thermosphere (MLT region) and later propagates downward [*Hoffmann et al*., 2007]. More sophisticated generations of models show that a doubled CO_2 concentration in the atmosphere indicates a cooling in the atmosphere everywhere above the tropopause. However, the smallest values of cooling occur around the mesopause [*Schmidt et al*., 2006]. These results make temperature trends and variations in the MLT region important to investigate further.

The MLT region is characterized by strong variability in winter temperatures. This is among others due to planetary and gravity wave activity and Sudden Stratospheric Warmings (SSW), which are coupling processes between the lower, middle, and upper atmosphere [*Funke et al*., 2010]. Solar flux variability is also believed to have an influence on variability of mesospheric temperatures, but how much influence is not fully agreed upon [*Beig et al*., 2008; 2012; *Huang and Brasseur*, 1993; *Schmidt and Brasseur*, 2006].

The hydroxyl airglow temperature series from Longyearbyen, Svalbard, is one of the longest continuous measurement records of hydroxyl (OH*) winter temperatures in the world. *Sigernes et al*. [2003] and *Dyrland and Sigernes* [2007] have earlier reported on trends and features of the temperature series from Longyearbyen. *Sigernes et al*. [2003] reported a close to zero trend for the period 1983 to 2001: +0.6 K ± 2.0 K/decade. *Dyrland and Sigernes* [2007] reported a slightly positive trend from the period 1983 to 2005: +2.0 K ± 1.0 K/decade.

This study, with the supplement of OH* airglow temperatures from the last eight winter seasons, gives an update on the mesospheric temperature trend above Longyearbyen, Svalbard. In section 2, we describe the instrument, the temperature retrieval method, and the calibration procedure. In section 3, trends are presented and discussed with regard to seasonal variations and solar cycle variability. A summary of the results is presented in section 4.

Table 1. Number of Data Points in Each Winter Season From 1983/84 to 2012/13[a]

1983/84	42	1993/94*	6	2003/04	85
1984/85	42	1994/95	15	2004/05	27
1985/86	48	1995/96	23	2005/06	31
1986/87	40	1996/97*	1	2006/07	22
1987/88	66	1997/98	35	2007/08	28
1988/89*	5	1998/99*	3	2008/09	54
1989/90	58	1999/00	47	2009/10	30
1990/91*	9	2000/01	57	2010/11	93
1991/92*	–	2001/02	29	2011/12	103
1992/93*	–	2002/03	35	2012/13	91

[a]Seasons with less than 10 days of retrieved data are noted with *. These seasons are excluded from the trend analysis.

2. Instrumentation and Data

2.1. Data and Measurement Technique

Measurements of OH* airglow intensities in Longyearbyen on a regular basis date back to 1980. Then OH* rotational temperatures were obtained from the OH*(8-3) band using a ½ m focal length Ebert-Fastie spectrometer. To gain spectral resolution, the instrument was replaced with a 1 m Ebert-Fastie spectrometer in 1983, scanning the P branch of the OH*(6-2) band. Temperatures derived from the airglow intensities are weighted averages from the height range of the vibrational state of OH*(6-2). The observing season is from the beginning of November to the end of February, and temperatures are retrieved as long as the Sun is more than 12° below the horizon. The spectrometer scans one spectrum every 25 s. Daily averaged temperatures are estimated for days with 3 or more hours of retrieved data. Seasonal averages are estimated for seasons with 10 or more days of retrieved data. The number of data points in each season contributing to the means is listed in Table 1.

The rotational temperatures were derived from hourly averaged measured spectra by calculating synthetic spectra as a function of instrumental band pass and temperature. The typical instrumental band pass is 5 Å. The background was detected by finding the optimal fit between the measured and synthetic spectra. The temperatures were derived from the slope of a linear fit to a Boltzmann plot using $P_1(2)$, $P_1(3)$, $P_1(4)$, and $P_1(5)$ rotational line intensities of the OH*(6-2) band. Also, the corresponding P_2 lines ($P_2(3)$, $P_2(4)$, and $P_2(5)$) were ensured to follow the same linear fit, although their intensities were not used for temperature retrieval. Using rotational temperatures to represent neutral air temperatures requires an assumption of local thermodynamical equilibrium (LTE) with the environment. Initially, the hydrogen-ozone reaction produces OH* in highly excited rotational states which are not in LTE, but through collisions the lower vibrational and rotational states can be thermalized. Given the collisional frequency and radiative lifetime the OH*($v = 6$) state is considered to have undergone enough collisions to conform to a Boltzmann distribution [*Sivjee and Hamwey*, 1987] and that the OH*(6-2) vibrational-rotational band can been considered in quasi-LTE, meaning rotational states with rotational quantum number < 6 follow the Boltzmann distribution, but higher levels do not [*Pendleton et al.*, 1993]. Following this, our choice to include the $P_1(N = 2)$ to $P_1(N = 5)$ lines in our analysis is validated. The conclusion that the OH*(6-2) band is thermalized has been questioned quite recently by *Cosby and Slanger* [2007] who found that rotational temperatures derived from low rotational line intensities show a strong dependence on vibrational level, with higher temperatures for higher vibrational levels. This difference in temperature is only partly explained by the fact that different vibrational levels have their peak emissions at different altitudes [*von Savigny et al.*, 2012]. The interpretation of OH* temperatures as absolute neutral air temperatures is therefore questionable, especially for higher rotational-vibrational levels, and we therefore limit our analysis to spectra that follow the Boltzmann distribution and that can be considered in quasi-LTE. To ensure this, we employ certain criteria for selection of good spectra which are described below.

Covariance between hourly averaged measured and synthetic spectra was calculated to remove spectra that were contaminated by aurora, which occur frequently at 78°N. Spectra with a very high background due to scattering of moonlight or artificial light by clouds were also filtered out. Spectra with a covariance between the measured and synthetic spectra less than 0.8 were discarded. In addition, the fit variance for P_1 and P_2 was calculated for every spectrum to ensure that the different rotational lines follow the Boltzmann distribution and thus are in (quasi) LTE with the environment. Spectra with P_1 fit variance greater than 0.05 and P_2 fit

variance greater than 0.3 were omitted from further analysis. These criteria for selecting good spectra have been chosen based on experience and consistency for the whole data set. Depending on the weather conditions and auroral activity of each winter, the fraction of hourly averaged spectra that are discarded from further analyses ranges between 50% and 88%.

Uncertainties were calculated for each hourly averaged spectrum from the error in the least-squares fit to the Boltzmann plot. The error in the daily averaged temperatures was calculated by weighting the hourly averaged temperatures according to their individual uncertainty [*Bevington and Robinson*, 1992]. The error of the daily averaged temperatures ranges between 0.2 and 5 K. A more detailed description of the instrument and the temperature retrieval method can be found in *Sigernes et al*. [2003].

The temperature retrieval of the whole Longyearbyen OH* temperature record was done using Einstein coefficients from *Mies* [1974]. Using different Einstein coefficients has been demonstrated to have a significant impact on estimated temperatures [e.g., *Perminov et al*., 2007], but since this paper concerns a trend assessment and relative variations within a temperature series, the choice of transition probabilities does not affect the result as long as the same set is used for the entire data set.

From 1980 to 2007, OH* airglow measurements were done at the Auroral Station in Adventdalen (78°N, 15°E), but in 2007 the spectrometer was moved to the new observatory, the Kjell Henriksen Observatory (KHO) (78°N, 16°E). The distance between the two sites is approximately 8 km. The instrument's field of view is approximately 5 degrees in the zenith direction. The cone angle is slightly larger in the direction parallel to the entrance slit. At 90 km altitude, this corresponds to an area of measurement of ~9×12 km. Differences in local weather conditions between the two sites are small [*Holmen et al*., 2014]; thus, there should be no geophysical reasons why the change of location has influenced the measured temperatures. Also, analysis of the spectral background shows that it did not change significantly after 2007. Thus, the moving of the spectrometer is considered to have no impact on the comparability of the OH* measurement series.

2.2. Calibration

The wavelengths measured by a spectrometer will drift slightly with time and environmental conditions. To ensure the accuracy of the measurements, periodic calibrations must be conducted. Sensitivity calibrations of the 1 m Ebert-Fastie spectrometer conducted in 1980, 2002, and 2004 are presented in *Sigernes et al*. [2003] and *Dyrland and Sigernes* [2007]. Calibrations have been performed yearly since 2007. *Dyrland and Sigernes* [2007] concluded that the instrument had been operating stably with no overall degradation in sensitivity from 1983 to 2004.

Operating a spectrometer stably over time is a continuous battle of upgrading software and electronics, including detector and counting circuit. The spectrometer has for instance changed operating system five times during its lifetime. This involves change of counter cards, high voltage supplies, pulse amplifier/discriminator (PAD), photomultiplier tube (PMT), and cooler. This will all affect the performance of the instrument. Fine tuning of mirror, grating, and slit position is also important for optical performance. Therefore, we conduct sensitivity calibrations yearly. Note that the optical and mechanical elements of the instrument have never been replaced.

The main components in the calibration of the spectrometer are a Lambertian diffusive screen (SRT-99-180, Spectralon®, Labsphere Inc.) and a lamp. The lamp acts as a point source to the screen, and the screen is the actual source of the calibration.

The spectral radiance of the screen is given by:

$$B(\lambda) = \rho(\lambda) \times M_0(\lambda) \times \left(\frac{z_0}{z}\right)^2 \times \cos\ \alpha \qquad \left[\frac{R}{\text{Å}}\right]$$

where $\rho(\lambda)$ is the reflectance factor of the Lambertian surface and is nearly constant throughout the near-infrared region of the spectrum ($\rho(\lambda) \approx 0.98$). z is the distance between the center of the screen and the lamp, and α is the angle between the Lambertian screen and the lamp axis. $M_0(\lambda)$ is the known irradiance of the lamp in Rayleigh per Ångström [R/Å], initially obtained at a distance z_0. The lamp irradiance certification is in units of $\text{mW/m}^{-2}\text{nm}$, but is converted to number of photons $\text{cm}^{-2}\,\text{s}^{-1}\,\text{sr}^{-1}$ and multiplied by $4\pi \times 10^{-6}$ to obtain the unit R/Å [*Sigernes et al*., 2007, 2012].

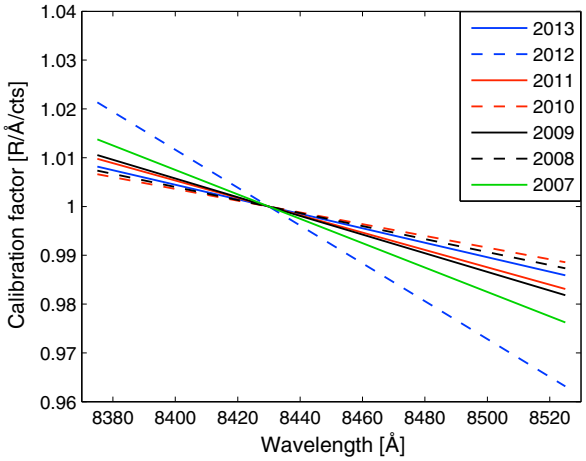

Figure 1. Spectrometer calibration factors for calibrations conducted from 2007 to 2013. Calibrations conducted from 2008 to 2013 were performed outdoors at the Kjell Henriksen Observatory (KHO) using a 200 W tungsten lamp. The 2007 calibration was conducted indoors in the optical lab at The University Centre in Svalbard, using a 45 W lamp.

The calibration factor of the instrument is given by:

$$K(\lambda) = \frac{B(\lambda)}{B(\lambda)} \qquad \left[\frac{R}{\text{Å}}/Cts\right]$$

where $C(\lambda)$ is the raw counts of the instrument produced by the illuminated screen. Calibration factors for calibrations performed from 2007 to 2013, normalized at the $P_1(3)$ line, are shown in Figure 1. The 2007 calibration was conducted indoors in the optical lab at The University Centre in Svalbard, without taking the plexiglass dome into account. A 45 W lamp (Oriel SN7-1633) was used. Since 2008, calibrations have been conducted outdoors at the KHO, using a 200 W tungsten lamp (Oriel SN7-1859).

Variation within the wavelength region from 8375 to 8525 Å and corresponding temperature uncertainties for the years 2007 to 2013 are shown in Table 2. Note that the spectral slopes of the calibration factors in the wavelength region are nearly constant through the years. It is a change in slope of the calibration factors that is important to the retrieval of the temperatures. The variation is within 4%, except for 2012, when the spectral slope was 5.3%. The reason for the higher variation in 2012 is not clear but could be weather related. The spectral slope of the calibration factors retrieved before and after the move of the instrument in 2007 did not change significantly. Temperature uncertainty as a consequence of the spectral slope was found by multiplying the calibration factors to synthetic spectra with constant background and zero slope, generated with temperatures ranging from 180 to 260 K. The temperatures derived from the spectra give an estimate of the temperature uncertainty due to the spectral slope. Temperature uncertainties range from 1 to 6 K. The absolute values of the calibration factors at 8430 Å ($P_1(3)$ line) are also listed in Table 2. The absolute value of the calibration factor varies by a factor of ~2 between 2009 and the latter years, and a factor of ~4 from that found by *Dyrland and Sigernes* [2007] for the earlier years.

It must be emphasized that our yearly calibration is a secondary calibration. The 200 W Tungsten lamp used for calibration outdoors is certified by comparing to our NIST (National Institute of Standards and Technology) traceable lamp source located in the calibration lab of The University Centre in Svalbard. Even though we have improved the secondary lamp housing to be more weather resistant and use lasers to measure distance, the outside temperature and wind conditions still affect the calibration outcome. A change in effective temperature is easily seen in the current running through the filament of the lamp. Snow and ice conditions near the instrument dome may also affect the setup of the Lambertian surface and the angle measurements. The above uncertainties are the main reasons for change in the level of the calibration factors in Table 2. Based on that the spectral slopes of the calibration factors are nearly constant through the years, we conclude that temperature measurements by the spectrometer are reliable for the time period 1983 to 2013.

Table 2. Calibration Output[a]

	Spectral Slope	Temperature Uncertainty	Absolute Value, 8430 Å
2013	2.4%	1–3 K	0.89
2012	5.3%	3–6 K	1.08
2011	2.9%	2–4 K	0.92
2010	1.6%	1–2 K	1.11
2009	1.5%	1–2 K	1.94
2008	1.7%	1–2 K	1.19
2007	3.7%	1–3 K	1.14

[a]Variation over the wavelength region 8375–8525 Å for years 2007 to 2013. The corresponding temperature uncertainties caused by the spectral slopes are also listed, together with the absolute values of the calibration factors at 8430 Å ($P_1(3)$ line).

The above procedure is our standard way of conducting secondary sensitivity calibrations of the Ebert-Fastie spectrometer. An improved method could be to use a portable low-light source and to monthly calibrate the instrument indoors, under its dome, reducing weather effects and logistics.

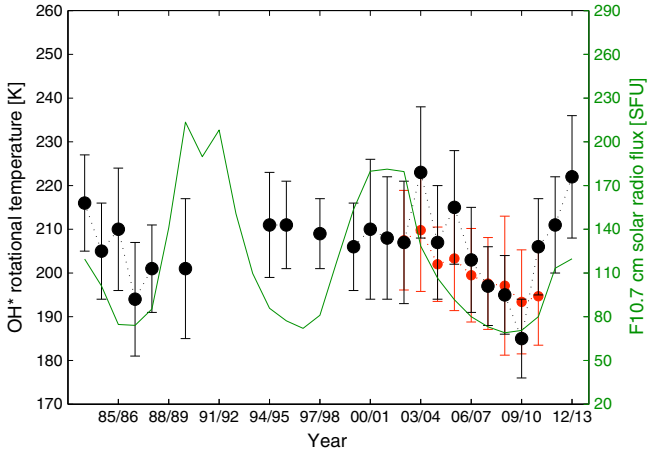

Figure 2. Seasonal averages of OH* temperatures before correction for seasonality and solar response. Seasonal averages are averages from November through February. Standard deviations are plotted as errorbars. Meteor radar temperatures at 90 km (November–February averages) from the NSMR radar in Longyearbyen are plotted as red bullets with standard deviations as errorbars. Variation of F10.7 cm solar radio flux during the same period is plotted as a green line.

3. Results and Discussion

There are many variables that can influence OH* temperatures. Sources of temperature variability are the mean meridional flow, planetary wave activity, solar flux variability, tides, gravity waves, and chemical processes like ozone depletion [*French and Klekociuk*, 2011; *Beig et al*., 2003]. These processes result in variations in OH* airglow temperatures on time scales ranging from minutes to decades. Also, variations in derived OH* temperatures may be influenced by changes in the altitude of the OH* layer. When investigating the long-term trend of a mesospheric temperature series, the goal is to identify factors influencing the natural variability and subtract their effects from the data set.

Uncorrected, seasonal averages of all winters in the Longyearbyen hydroxyl airglow temperature series are plotted in Figure 2 and reveal that there were some cold winter seasons in the period from 2008 to 2010. Temperatures retrieved from meteor trail echoes at 90 km altitude from the Nippon/Norway Svalbard Meteor Radar (NSMR) located in Adventdalen near Longyearbyen show a decrease in the same time period. Figure 2 shows that the meteor radar temperatures follow the variations in the airglow temperatures reasonably well, even though the magnitude of the variations is smaller. A period of lower temperatures around 2008 to 2010 can also be recognized in data from the Davis station in Antarctica, though not of the same magnitude [*French and Klekociuk*, 2011]. The solar activity was at a minimum during that time and the solar minimum around 2008 was the weakest solar minimum in nearly 100 years [*Ahluwalia and Jackiewicz*, 2011]. OH* temperatures are correlated reasonably well with solar activity over the most recent solar minimum. It is hard to see the same coincident pattern over the solar minimum around 1996. The temperature over the 1989/1990 winter is at odds with the solar maximum during that period, and temperatures around 1999 to 2003 do not appear to increase with the 2001 solar maximum. Reasons for this will be discussed in section 3.3.

In section 3.1, we explain how the mean climatology is removed from the time series to subtract the effect of seasonal variations from the data set. In section 3.2, solar cycle dependence is investigated. In section 3.3, the new and updated long-term trend is presented and discussed in terms of sources of temperature variability and changes in the altitude of the OH* layer. The trend is also compared with the previous trend update and trends from other sites. Monthly trends are evaluated in section 3.4.

3.1. Subtraction of Climatology

The seasonal variation is largely a result of the mean meridional flow. The method described in *French and Klekociuk* [2011] and *Azeem et al*. [2007] was used to subtract effects of seasonal variations from the data set. First, the time series was superposed by day of year, and daily averages for the same day of year were calculated. Then a 5-day running mean of these daily averages was applied. The running mean values obtained were then considered to be the mean winter climatology. To remove the effects of seasonal variations from the temperature record, the mean climatology for each day of year was subtracted from each daily temperature in the data set. The superposed temperatures with the 5 day running mean are shown in Figure 3. A more detailed description of the seasonal variations in the Longyearbyen OH* temperature data set can be found in *Holmen et al*. [2014].

Seasonal averages of the residual temperatures were estimated as the mean of daily averaged temperatures measured from November through February. Earlier trend estimates on the temperature record have used

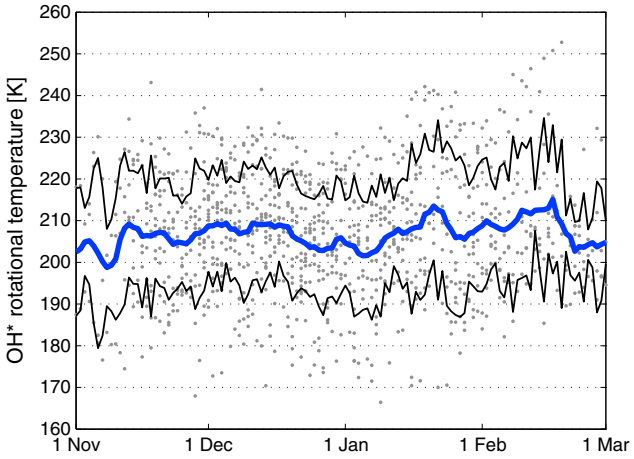

Figure 3. Superposition of the Longyearbyen OH* temperatures by day of year. Grey dots are the daily averaged OH* temperatures and the black lines represent ± 1 standard deviation. The blue line is the 5-day running mean.

the average of December and January as the seasonal average, but since the temperatures are now corrected for seasonal variations we choose to include the whole data set.

3.2. Solar Cycle Dependence

According to most recent studies on mesospheric long-term trend assessments, solar activity is believed to have an effect on mesospheric temperatures [e.g., *Azeem et al*., 2007; *Offermann et al*., 2010]. To subtract the effect from the data set we must know the level of influence. When it comes to irradiance and appearance, several measures of solar variation exist. In this paper, three different measures have been used to investigate solar dependence on OH* temperatures: The 11 year sunspot cycle (SSN), the F10.7 cm solar radio flux and total solar irradiance (TSI). The 11-year solar cycle is the periodic variation of the number of sunspots on the Sun. Records of the daily sunspot number are freely available from Solar Influences Data Analysis Center (SIDC). The F10.7 cm solar flux is a measure of the solar radio flux per unit frequency at a wavelength of 10.7 cm, near the peak of the observed solar radio emission. The global daily value of this index is measured at local noon at the Penticton Radio Observatory in Canada, and it has been measured daily since 1947. It is freely available on the webpage of National Geophysical Data Center (NGDC), a part of the National Oceanic and Atmospheric Administration (NOAA). The total solar irradiance is the spatially and spectrally integrated solar radiation incident at the top of the Earth's atmosphere. The time series used is the Active Cavity Radiometer Irradiance Monitor (ACRIM) composite, available at the ACRIM web page.

A solar response coefficient can be defined as how many Kelvin of the measured mesospheric temperatures that are accredited variability in solar activity. This coefficient can be estimated by the linear fit to a scatterplot of OH* residual temperatures against the different measures of solar activity. The slope of the linear fit is the solar response coefficient. Solar forcing, correlations, and 95% confidence limits for all three measures of solar activity

Table 3. Solar Forcing[a]

	Pearson's *r*	Solar Forcing	95% Confidence Intervals
F10.7 cm			
Daily average	0.12*	3.7 K ± 0.9 K/100 SFU	+1.9 K < S < +5.5 K
Monthly average	0.21^	4.4 K ± 2.4 K/100 SFU	−0.3 K < S < +9.1 K
Monthly average minus SSW	0.25^	5.1 K ± 2.7 K/100 SFU	−0.4 K < S < +10.6 K
Seasonal average	0.20	3.6 K ± 4.0 K/100 SFU	−4.7 K < S < +11.9 K
Total solar irradiance (TSI)			
Daily average	0.15*	3.7 K ± 0.8 K/Wm^{-2}	+2.2 K < S < +5.2 K
Monthly average	0.27*	4.8 K ± 2.1 K/Wm^{-2}	+0.7 K < S < +8.9 K
Monthly average minus SSW	0.32*	6.5 K ± 2.6 K/Wm^{-2}	+1.2 K < S < +11.9 K
Seasonal average	0.29	4.5 K ± 3.2 K/Wm^{-2}	−2.5 K < S < +10.8 K
Sunspot cycle			
Daily average	0.11*	3.3 K ± 0.9 K/100 spots	+1.5 K < S < +5.0 K
Monthly average	0.20^	4.5 K ± 2.5 K/100 spots	−0.4 K < S < +9.4 K
Monthly average minus SSW	0.17	3.6 K ± 2.8 K/100 spots	−2.0 K < S < +9.1 K
Seasonal average	0.20	4.0 K ± 4.3 K/100 spots	−4.9 K < S < +12.9 K

[a]Correlations, solar forcing coefficients, and 95% confidence limits calculated for three different measures of solar activity against the seasonally corrected OH* residuals. The solar forcing coefficients for the seasonal averages are computed using multivariate regression. Note the different units on the solar forcing coefficients. *: correlation at better than 95% significance. ^: correlation at better than 90% significance.

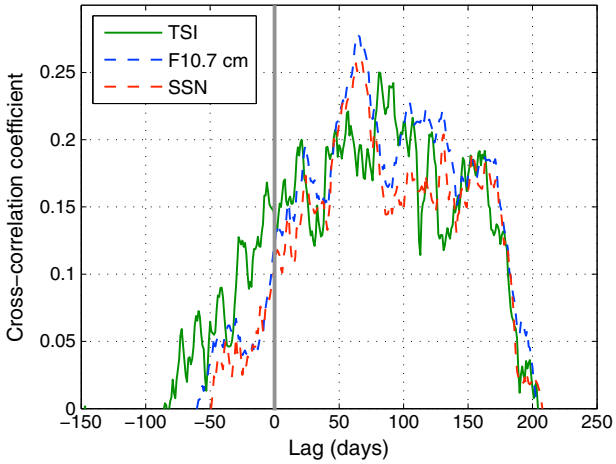

Figure 4. Lag-correlation analysis of daily averaged temperature residuals with corresponding daily values of total solar irradiance (TSI), F10.7 cm solar radio flux, and the sunspot number.

are listed in Table 3. The temperature residuals were averaged over a monthly and seasonal time scale. By averaging over a monthly time scale, the effect of planetary wave variability is reduced. SSWs are events caused by planetary waves and may last for several weeks. Since these events apparently have a significant influence on mesospheric temperatures [*Hoffmann et al*., 2007], months where SSWs were present were excluded to see if that made any difference. SSW periods were identified using reanalysis temperatures and winds provided through the Modern-Era Retrospective analysis for Research and Applications (MERRA) project, available as annual meteorological statistics at the NASA webpage.

The highest correlation was achieved for the OH* residuals against the TSI but only slightly better than for the F10.7 cm solar flux and SSN. It is hard to say why the correlation was highest between TSI and the temperature residuals. Correlation between SSN and the OH* residuals may be biased by that even though the number of sunspots may be zero for many days in a row, the OH* temperatures still vary. The correlations are overall lower than correlations achieved for some other high-latitude sites [*Azeem et al*., 2007; *French and Klekociuk*, 2011]. The correlation increases slightly when excluding SSW months, except for SSN. By eliminating SSW months, we are left with a data set that is dynamically quieter. This is not representative for average conditions. Therefore, we do not exclude SSW periods in further analyses.

There may be a phase difference between solar input and solar response. This can affect the magnitude of the solar response coefficient [*Wynn and Wickwar*, 2009; *French and Klekociuk*, 2011]. A cross-correlation analysis was performed to check if the correlation improved when a time lag was applied to the data sets. Lag correlation of the daily residuals with daily TSI, F10.7 cm solar flux and SSN is shown in Figure 4. Peak correlation for the association of TSI and temperature occurs at a lag of ~80 days. The correlation coefficients between the residuals and both F10.7 and SSN peaks at where the solar activity measures lead the temperature by ~65 days. At this point, F10.7 correlation ($r = 0.28$) exceeds both SSN and TSI correlation. By applying a 65 day lag between the daily residuals and the corresponding F10.7 data, the solar response coefficient becomes 8.8 K ± 0.9 K/100 solar flux units (SFU). This is a significantly higher response than at zero lag. By applying the same time lag to the monthly averaged residuals and F10.7, the solar response is 6.4 K ± 2.3 K/100 SFU, also higher than at zero lag.

French and Klekociuk [2011] found a time lag between solar input and OH* temperature response of ~160 days. *Shapiro et al*. [2012] found highest correlations between tropical mesospheric OH* and Lyman-α irradiance at about zero time lag. The zero time lag was justified by the short lifetime of OH*. According to *Wynn and Wickwar* [2009], it is reasonable to have phase lags between the solar input and the atmospheric response of up to several years at 90 km height. It is hard to find a plausible explanation for why the correlations are higher at lags of ~65 and ~80 days. Since we do not have continuous airglow measurements for all days or months in the winter seasons from 1983 to 2013 the lag-correlation analysis must be evaluated with caution.

A solar response around 4 K/100 SFU retrieved with the F10.7 cm index is comparable with what is reported for other locations in polar regions and midlatitudes during the last decade [*She and Krueger*, 2004; *Azeem et al*., 2007; *Offermann et al*., 2010; *French and Klekociuk*, 2011]. *Schmidt et al*. [2006] reported that temperature response in the mesopause to the solar cycle lies between 2 and 10 K. However, *Hall et al*. [2012] found a solar response coefficient of 16 K/100 SFU for the temperature series derived from the NSMR radar in Adventdalen, Longyearbyen. This is significantly higher than our response coefficient. It is likely that the main explanation for the large difference is the difference in time span of the two temperature series. While the OH* temperatures go back to 1983, the meteor radar temperatures go back to 2001. When only taking the OH*

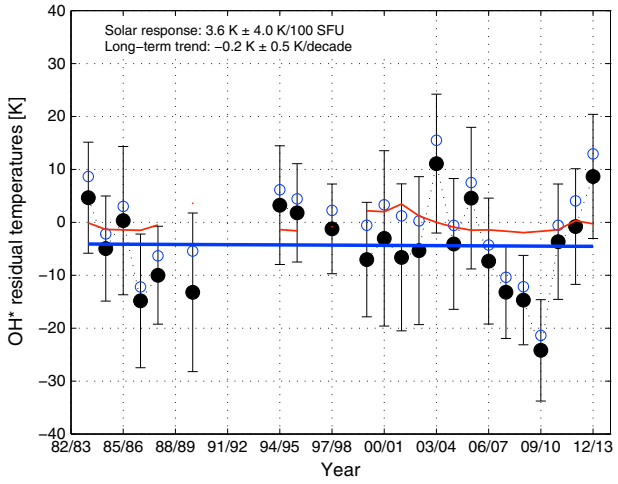

Figure 5. Hydroxyl (OH*) residual temperatures from Longyearbyen, 1983–2013, corrected for seasonal variations and solar response. Standard deviations are plotted as errorbars. Blue circles are seasonally averaged residuals corrected for climatology. The red line is the multivariate fit to the climatologically corrected residuals of the form $Fit_T = Y.Trend + S.F107 + const$. Seasonal averages corrected also for solar response are plotted as black bullets with standard deviations as errorbars. The blue line is the linear long-term trend.

temperatures from 2001 to 2011 into consideration, we get a solar response coefficient of 10.9 K/100 SFU. This is significantly higher than the coefficient estimated for the whole time period but still less than what was found by *Hall et al.* [2012]. A 10.9 K/100 SFU response is within the 95% confidence interval for the solar forcing of the overall fit to the data by F10.7 cm (see Table 3).

Sigernes et al. [2003] reported that there seemed to be no connection between the F10.7 cm flux and the OH* temperatures for the Longyearbyen data set from 1983 to 2001. Calculating the solar response coefficient for this time period gives a result that is close to 0 K/100 SFU. The length of the time series may be a reason for this. A long time series is required to assure a reliable result. The zero response from 1983 to 2001 is within the 95% confidence interval of the overall fit to the data.

Offermann et al. [2010] raise the question whether the solar response coefficient obtained by a linear fit between temperature and solar flux index gives an optimal approximation of the true value. They argued that the length of the time series at least had to be longer than one solar cycle, but even a long time series gives no guarantee for a correctly determined solar response coefficient.

3.3. Updated Trend, 1983–2013

A multivariate regression fit of the form $Fit_{temp} = Y.Trend + S.F107 + const$ was made to detect the long-term coefficient coupled with the solar cycle coefficient. This was done to take both parameters into account simultaneously. Figure 5 shows the multivariate fit to the seasonal temperatures with climatology removed, with no F10.7 lag.

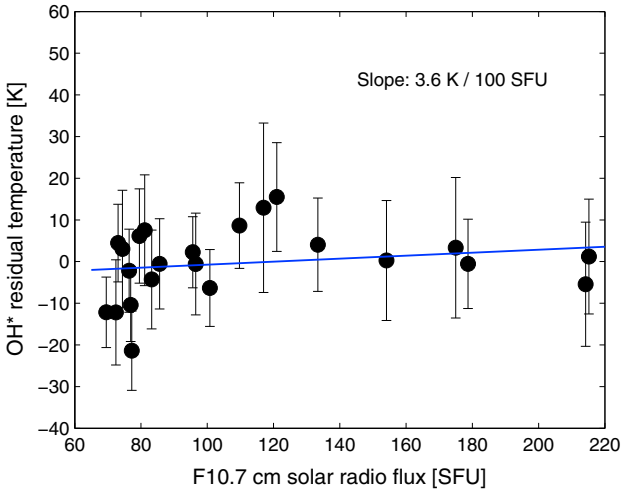

Figure 6. Scatterplot of the seasonally averaged temperatures against the corresponding F10.7 cm solar flux values. Standard deviations are plotted as errorbars. The blue line is the linear fit to the data.

Figure 6 shows a scatterplot of the seasonally averaged temperatures against the corresponding F10.7 cm solar flux values. The decoupled solar cycle component is 3.6 K ± 4.0 K/100 SFU. Figure 5 shows the decoupled long-term trend component. The uncertainty of the trend was estimated by removing 1 year at the time from the time window and estimating trends based on the remaining data points. This is commonly referred to as the bootstrap method. The standard deviation of the trends was considered the overall uncertainty [*Efron and Tibshirani*, 1993]. The long-term temperature trend is −0.2 K ± 0.5 K/decade. By performing a multivariate regression analysis with TSI values, which gave a higher correlation with the residuals at zero lag, the solar response coefficient is 4.2 K ± 3.2 K/Wm^{-2}.

Table 4. Seasonal and Monthly Trends

	Linear Trend	95% Confidence Intervals
Seasonal (F10.7 cm)	−0.2 K ± 0.5 K/decade	−4.2 K < Y < +4.0 K
Seasonal (TSI)	−0.7 K ± 0.5 K/decade	−4.9 K < Y < +3.4 K
November	+4.5 K ± 1.1 K/decade	−2.6 K < Y < +11.5 K
December	−2.9 K ± 0.5 K/decade	−7.0 K < Y < +12.2 K
January	+1.4 K ± 0.6 K/decade	−4.3 K < Y < +7.1 K
February	+2.9 K ± 1.0 K/decade	−6.4 K < Y < +12.2 K

The corresponding long-term trend is −0.7 K ± 0.5 K/decade. Ninety-five percent confidence limits for the seasonal trends are listed in Table 4.

There is variability in the temperature data set that is not accounted for by the seasonal variation or the solar cycle and long-term trend component. The regression fit is not an optimal fit to the residual temperatures. Around the cold period from 2008 to 2010, the difference between the regression fit and the seasonally averaged residual temperatures is between 10 and 20 K. The remaining variability may be explained by, e.g., planetary waves, gravity waves, SSWs, and instrument calibration uncertainty. SSWs occur quite often in the Northern Hemisphere and are believed to be connected with mesospheric processes [*Hoffmann et al*., 2007]. During the 1980s and after 2000, a large number of SSWs were detected (close to one major or minor warming per Arctic winter). As a contrast, very few SSWs were detected in the 1990s [*Kuttipurath and Nikulin*, 2012]. In the Southern Hemisphere, only one SSW has ever been observed. This occurred in September 2002 [*Peters et al*., 2007]. This may help explain why the variability in OH* temperatures is much larger in our data compared to, e.g., data from the Davis and the Amundsen-Scott South Pole stations. Gravity wave activity may be a source of temperature variability. However, both the Davis and the Amundsen-Scott stations experience substantial gravity wave activity [*Beldon and Mitchell*, 2009]. The remaining variability in temperatures not accounted for by the multivariate fit is thus not completely understood.

Another factor that can affect temperature variations and trends is changes in the altitude of the OH* layer. The height profile of the hydroxyl emission is determined by the shape of the bottom side of the atomic oxygen emission, i.e., the atomic oxygen scale height relative to that of the neutral atmosphere [*Beig et al*., 2003]. The peak altitude is controlled mainly by the rate of downward diffusion and gravity waves, tides, and planetary-scale disturbances which cause vertical motion of the peak. There is an inverse correlation between OH* altitude and integrated emission rate, and the brightness/intensity increases as the altitude decreases [e.g., *Liu and Shepherd*, 2006]. Thus, the hydroxyl rotational temperature corresponds, in general, neither to the temperature at a particular altitude nor to a particular pressure surface. Still, it is considered a good proxy for the temperature at the peak altitude [*Beig et al*., 2003].

The peak altitude of the OH* layer has been established by rocket and satellite measurements and is generally considered to be 87 km with a full width at half maximum (FWHM) of 8 km [*Baker and Stair*, 1988]. However, recent satellite measurements from polar latitudes have shown that the peak altitude of the OH* emissions can range from 75 to >90 km, particularly during winters when the polar vortex is disturbed and SSWs occur [*Winick et al*., 2009]. They also found that there is a longitudinal asymmetry depending on the position of the polar vortex. Furthermore, the peak altitude also varies with the upper vibrational level of the transition, and a recent paper found that it changes by about 0.5 km per vibrational level, the higher vibrational levels peaking at a higher altitude [*von Savigny et al*., 2012]. Since our paper presents data from only one vibrational band, the latter is not important to consider for this study.

For the Svalbard data, the inverse relationship between OH* peak altitude and emission rate/temperature has been verified using data from the winter season 2003–2004 [*Mulligan et al*., 2009], when the OH* layer peak altitude ranged from 76 to 90 km during a period of a highly disturbed circulation system over the Arctic. The low altitudes were attributed to downwelling due to the strengthening of the polar vortex after an SSW in January–February 2004 [*Dyrland et al*., 2010]. A temperature increase of the order of 15 K was attributed to the lowering of the layer, so the altitude is definitely a key factor in determining the OH* temperature [*Dyrland et al*., 2010]. Similarly, low OH* peak altitudes were observed after the SSW in 2006 [*Winick et al*., 2009]. Whether the relatively low temperatures from 2008 to 2010 can be connected to an unusually high OH* peak would be very interesting to study but is beyond the scope of this paper. To verify this, we would need satellite data overlapping our data. The only instrument that could provide this is SABER (Sounding of the Atmosphere using Broadband Emission Radiometry) on the TIMED (Thermosphere Ionosphere Mesosphere Energetics Dynamics) satellite. However, these data would only be

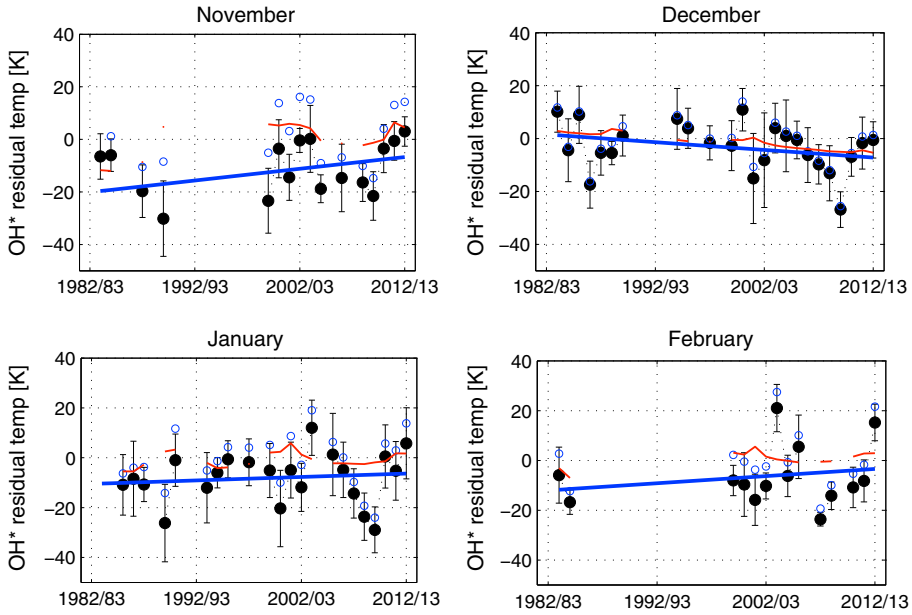

Figure 7. Monthly trends for November through February. Blue, hollow circles represent seasonally corrected residual temperatures. Red lines represent multivariate fits to the residuals. Monthly hydroxyl (OH*) temperatures corrected for both seasonal variations and solar response is plotted as black bullets, with standard deviations as errorbars. Blue lines are linear trends.

available for the latter part of the time series. Alternatively, the peak altitude could be modeled following the empirical measurements of OH* band intensity [*Mulligan et al.*, 2009; *Liu and Shepherd*, 2006]. However, the limited accuracy of the sensitivity calibrations (due to reasons mentioned in section 2.2: weather conditions, temperature, lamp currents etc.) makes it very difficult to verify the absolute intensity values for the data.

Compared to the last trend analysis done by *Dyrland and Sigernes* [2007], the new trend is now negative, but not significantly different from zero. The seasonally adjusted temperature residuals in, e.g., the 2009/2010 winter season is close to 10 K colder than for any of the other seasons. The period of lower temperatures around 2008 to 2010 contributes to that the trend is a near-zero trend, compared to the slightly positive trend found by *Dyrland and Sigernes* [2007].

Hall et al. [2012] found a negative trend of $-4\,\mathrm{K} \pm 2\,\mathrm{K}$/decade for the meteor radar temperatures from Longyearbyen. The reason for the large difference in trend is partly explained by the difference in solar response due to the time span of the two data sets and the fact that the meteor radar temperatures are recorded all year-round. Therefore, also summer trends are included in the meteor radar temperature trend. Some studies indicate that negative temperature trends in the mesosphere are most evident during summer, but others disagree [*Lübken*, 2000; *Bremer and Berger*, 2002; *Beig et al.*, 2008]. Also, the OH* emission peak altitude is slightly different from the altitude for maximum echo occurrence rate observed by the meteor radar [*Hall et al.*, 2012].

Other studies on long-term mesospheric temperature trends from midlatitude and high-latitude sites report mostly negative or near-zero trends. *Semenov* [2000] found a negative trend of $-9.2\,\mathrm{K} \pm 0.8$ K/decade for the winter mesosphere over several stations at midlatitudes. Temperatures were derived from rocket soundings, OH* airglow, lidar measurements, and interferometric measurements of oxygen emissions. *Reisin and Scheer* [2002] also reported a negative trend, $-10.5\,\mathrm{K} \pm 0.8\,\mathrm{K}$/decade, for airglow temperatures measured at El Leoncito (32°S, 69°W). The more recent study of *Offermann et al.* [2010] showed a trend of $-2.3\,\mathrm{K} \pm 0.6\,\mathrm{K}$/decade from the OH* temperature series from Wuppertal (51°N, 7°E). Studies from high-latitude sites show no clear pattern. *French and Klekociuk* [2011] reported a trend of $-1.2\,\mathrm{K} \pm 0.9\,\mathrm{K}$/decade for the Davis station (68°S, 78°E) in Antarctica for the period 1995 to 2011. *Azeem et al.* [2007] reported a trend of $+1.0\,\mathrm{K} \pm 2.0\,\mathrm{K}$/decade for the period 1994 to 2004 for the South Pole Station (90°S). Model simulations of the mesopause region indicate trends usually below 1 K/decade [*Beig et al.*, 2003]. Our trend is in line with this.

3.4. Monthly Trends

Monthly trends give an understanding of the seasonal variability of trends. Monthly averages were estimated for months with 4 or more days of retrieved data. Trends were estimated making multivariate regression fits. Uncertainties were calculated using the bootstrap method. Figure 7 shows the monthly residuals, multivariate fits, and linear trends for November through February. Trends and 95% confidence limits for all 4 months are listed in Table 4. The same pattern as for the data series as a whole, with low temperatures from 2008 to 2010, can also be seen in the monthly averages.

All monthly trends are positive, except for December. However, the 95% confidence intervals do not rule out negative trends for November, January, and February, or a positive trend for December.

Offermann et al. [2010] found negative trends for December, January, and February, while the trend for November was close to zero. *French and Klekociuk* [2011] found a trend close to zero for May, June, and July (corresponding to November, December, and January in the Northern Hemisphere) and a cooling trend for August (corresponding to February in NH). There seem to be few similarities between their monthly trends and ours. This indicates that there are high uncertainties, but also that the OH* layer in different parts of the world is influenced differently by gravity and planetary waves, solar variability, etc.

4. Summary and Conclusions

In this study, the long-term trend of the currently 30 year long hydroxyl airglow temperature series from Longyearbyen is updated. The mean climatology was subtracted from the data set to remove effects from seasonal variations. In the previous trend updates, the winter average has been calculated from temperatures from December and January, but since the temperatures in this paper have been seasonally corrected also November and February temperatures are included. Solar cycle dependence was investigated by looking into three different measures of solar variation; the F10.7 cm solar radio flux, the sunspot number, and the total solar irradiance. Highest correlation was achieved for OH* temperatures against TSI but only slightly better than for F10.7 and SSN. A solar response coefficient of around 4 K/100 SFU was obtained from the slope of linear fits to scatterplots of the temperature residuals against the F10.7 cm solar radio flux.

A lag-correlation analysis was performed on the data set to check for correlation improvement when a time lag was applied. Peak correlation for OH* temperatures and F10.7 occurred at a lag of ~65 days. At this point, F10.7 correlation exceeded SSN and TSI correlations. The lag-correlation analysis must be evaluated with caution since the data set is not continuous.

A multivariate regression fit of the form $Fit_{temp} = Y.Trend + S.F107 + const$ was made to detect long-term trend coupled with solar response. Decoupled solar response is 3.6 K ± 4.0 K/100 SFU, and the updated long-term trend of the Longyearbyen hydroxyl temperature series is −0.2 K ± 0.5 K/decade. Cold winter seasons between 2008 and 2010 turn the new trend slightly negative compared to the previous trend update by *Dyrland and Sigernes* [2007]. The cold winters occurred during a period of solar minimum, and this solar minimum is the weakest registered in nearly 100 years. Temperatures from the NSMR radar near Longyearbyen show the same tendency as the airglow temperatures.

There is variability in the data set not accounted for by seasonal variation or the solar cycle and long-term trend components. Remaining variability may be caused by planetary waves, gravity waves, and SSWs, but this issue is not fully understood. Also, changes in the altitude of the OH* layer can affect temperature variations. The peak altitude of the OH* emissions can change particularly during winters when the polar vortex is disturbed and SSWs occur.

The recent trend analysis on temperatures at 90 km altitude using meteor radar observations from Longyearbyen by *Hall et al.* [2012] shows a more negative trend and a stronger solar response for the meteor radar temperatures. One reason may be the different lengths of the time series. Our trend is in line with climate models that predict only small changes in temperature in the mesopause region with increasing CO_2 emissions [*Beig et al.*, 2003].

Monthly trends were also evaluated using multivariate regression fits. The analysis reveals that trends for November, January, and February are positive, while the December trend is negative. However, 95% confidence intervals do not rule out a positive December trend and negative trends for the other winter months.

Acknowledgments

This work was financially supported by The Research Council of Norway through contract 223252/F50 (CoE) and the projects named: Norwegian and Russian Co-operation on Svalbard part 2 (196173/S30, NORUSCA2), Infrastructure for Space Physics related Research on Svalbard (195385, INFRASPACE), and High-Arctic Gravity waves and their impact on middle atmospheric circulation and temperature (204993). The authors wish to thank Chris Hall at Tromsø Geophysical Observatory, Norway, and Masaki Tsutsumi at the National Institute of Polar Research, Japan, for providing temperatures from the Nippon-Norway Svalbard Meteor Radar. Inquiries about calculated airglow temperatures used for this paper can be addressed to Fred Sigernes, The University Centre in Svalbard (freds@unis.no). Records of the daily sunspot number, F10.7 cm solar radio flux and total solar irradiance are freely available from the Solar Influences Data Analysis Center (SIDC), the National Geophysical Data Center (NGDC), and the Active Cavity Radiometer Irradiance Monitor (ACRIM), respectively.

References

Ahluwalia, H. S., and J. Jackiewicz (2011), Sunspot cycle 23 descent to an unusual minimum and forecasts for cycle 24 activity, *Adv. Space Res.*, *50*, doi:10.1016/j.asr.2011.04.023.

Akmaev, R. A., and V. I. Fomichev (1998), Cooling of the mesosphere and lower thermosphere due to doubling of CO_2, *Ann. Geophys.*, *16*, 1501–1512.

Akmaev, R. A., and V. I. Fomichev (2000), A model estimate of cooling in the mesosphere and lower thermosphere due to the CO_2 increase over the last 3-4 decades, *Geophys. Res. Lett.*, *27*(14), 2113–2116, doi:10.1029/1999GL011333.

Azeem, S. M. I., G. G. Sivjee, Y.-I. Won, and C. Mutiso (2007), Solar cycle signature and secular long-term trend in OH airglow temperature observations at South Pole, Antarctica, *J. Geophys. Res.*, *112*, A01305, doi:10.1029/2005JA011475.

Baker, D. J., and A. T. Stair Jr. (1988), Rocket measurements of the altitude distribution of the hydroxyl airglow, *Phys. Scripta*, *37*, 611–622.

Beig, G., et al. (2003), Review of mesospheric temperature trends, *Rev. Geophys.*, *41*(4), 1015, doi:10.1029/2002RG000121.

Beig, G., J. Scheer, M. G. Mlynczak, and P. Keckhut (2008), Overview of the temperature response in the mesosphere and lower thermosphere to solar activity, *Rev. Geophys.*, *46*, RG3002, doi:10.1029/2007RG000236.

Beig, G., S. Fadnavis, H. Schmidt, and G. P. Brasseur (2012), Inter-comparison of 11-year solar cycle response in mesospheric ozone and temperature obtained by HALOE satellite data and HAMMONIA model, *J. Geophys. Res.*, *117*, D00P10, doi:10.1029/2011JD015697.

Beldon, C. L., and N. J. Mitchell (2009), Gravity waves in the mesopause region observed by meteor radar, 2: Climatologies of gravity waves in the Antarctic and Arctic, *J. Atmos. Sol. Terr. Phys.*, *71*, 875–884, doi:10.1016/j.jast.2009.03.009.

Bevington, B. R., and D. K. Robinson (1992), *Data Reduction and Error Analysis for the Physical Sciences*, McGraw-Hill, New York.

Brasseur, G., and M. H. Hitchman (1988), Stratospheric response to trace gas pertubations: Changes in ozone and temperature distributions, *Science*, *240*, 634–637.

Bremer, J., and U. Berger (2002), Mesospheric temperature trends derived from ground-based LF phase-height observations at mid-latitudes: comparison with model simulations, *J. Atmos. Sol. Terr. Phys.*, *64*, 805–816.

Cosby, P. C., and T. G. Slanger (2007), OH spectroscopy and chemistry investigated with astronomical sky spectra, *Can. J. Phys.*, *85*, 77–99, doi:10.1139/P06-088.

Dickinson, R. E., and R. J. Cicerone (1986), Future global warming from atmospheric trace gases, *Nature*, *319*, 109–115.

Dyrland, M. E., and F. Sigernes (2007), An update on the hydroxyl airglow temperature record from the Auroral Station in Adventdalen, Svalbard (1980-2005), *Can. J. Phys.*, *85*(2), 143–151, doi:10.1139/P07-040.

Dyrland, M. E., F. J. Mulligan, C. M. Hall, F. Sigernes, M. Tsutsumi, and C. S. Deehr (2010), Response of OH airglow temperatures to neutral air dynamics at 78°N, 16°E during the anomalous 2003–2004 winter, *J. Geophys. Res.*, *115*, D07103, doi:10.1029/2009JD012726.

Efron, B., and T. Tibshirani (1993), *An introduction to the bootstrap*, Chapman and Hall, New York.

French, W. J. R., and A. R. Klekociuk (2011), Long-term trends in Antarctic winter hydroxyl temperatures, *J. Geophys. Res.*, *116*, D00P09, doi:10.1029/2011JD015731.

Funke, B., M. López-Puertas, D. Bermejo-Pantaleón, M. Garcia-Comas, G. P. Stiller, T. von Clarmann, M. Kiefer, and A. Linden (2010), Evidence for dynamical coupling from the lower atmosphere to the thermosphere during a major stratospheric warming, *Geophys. Res. Lett.*, *37*, L13803, doi:10.1029/2010GL043619.

Hall, C. M., M. E. Dyrland, M. Tsutsumi, and F. J. Mulligan (2012), Temperature trends at 90 km over Svalbard, Norway (78°N 16°E), seen in one decade of meteor radar observations, *J. Geophys. Res.*, *117*, D08104, doi:10.1029/2011JD017028.

Hoffmann, P., W. Singer, D. Keuer, W. K. Hocking, M. Kunze, and Y. Murayama (2007), Latitudinal and longitudinal variability of mesospheric winds and temperatures during stratospheric warming events, *J. Atmos. Sol. Terr. Phys.*, *69*, 2355–2366.

Holmen, S. E., M. E. Dyrland, and F. Sigernes (2014), Mesospheric temperatures derived from three decades of hydroxyl airglow measurements from Longyearbyen, Svalbard (78°N), *Acta Geophys.*, *62*(2), 302–315, doi:10.2478/s11600-013-0159-4.

Huang, T. Y. W., and G. P. Brasseur (1993), Effect of long-term variability in a two-dimensional interactive model of the middle atmosphere, *J. Geophys. Res.*, *98*(D11), 20,413–20,427, doi:10.1029/93JD02187.

Kuttipurath, J., and G. Nikulin (2012), A comparative study of the major sudden stratospheric warmings in the Arctic winters 2003/2004-2009/2010, *Atmos. Chem. Phys.*, *12*, 8115–8129, doi:10.5194/acp-12-8115-2012.

Liu, G., and G. G. Shepherd (2006), An empirical model for the altitude of the OH nightglow emission, *Geophys. Res. Lett.*, *33*, L09805, doi:10.1029/2005GL025297.

Lübken, F.-J. (2000), Nearly zero temperature trend in the polar summer mesosphere, *Geophys. Res. Lett.*, *27*(21), 3603–3606, doi:10.1029/2000GL011893.

Mies, F. H. (1974), Calculated vibrational transition probabilities of OH($X_2\Pi$), *J. Mol. Spectrosc.*, *53*, 150–188.

Mulligan, F. J., M. E. Dyrland, F. Sigernes, and C. S. Deehr (2009), Inferring hydroxyl layer peak heights from ground-based measurements of OH(6-2) band integrated emission rate at Longyearbyen (78°N, 16°E), *Ann. Geophys.*, *27*, 4197–4205.

Offermann, D., P. Hoffmann, P. Knieling, R. Koppmann, J. Oberheide, and W. Steinbrecht (2010), Long-term trends and solar cycle variations of mesospheric temperature and dynamics, *J. Geophys. Res.*, *115*, D18127, doi:10.1029/2009JD013363.

Pendleton, W. R., P. J. Espy, and M. R. Hammond (1993), Evidence for non-local-thermodynamical-equilibrium rotation in the OH nightglow, *J. Geophys. Res.*, *98*(A7), 2156–2202, doi:10.1029/93JA00740.

Perminov, V. I., A. I. Semenov, and N. N. Shefov (2007), On Rotational Temperature of the Hydroxyl Emission, *Geomagn. Aeron.*, *47*(6), 756–763, doi:10.1134/S0016793207060084.

Peters, D., P. Vargin, and H. Koernich (2007), A study of the zonally asymmetric tropospheric forcing of the austral vortex splitting during September 2002, *Tellus*, *59A*, 384–394, doi:10.1111/j.1600-0870.2007.00228.x.

Reisin, E. R., and J. Scheer (2002), Searching for trends in mesopause region airglow intensities and temperatures at El Leoncito, *Phys. Chem. Earth*, *27*, 563–569.

Schmidt, H., and G. P. Brasseur (2006), The response of the middle atmosphere to solar cycle forcing in the Hamburg Model of the Neutral and Ionized Atmosphere, *Space Sci. Rev.*, *125*, 345–356, doi:10.1007/s11214-006-9068-z.

Schmidt, H., G. P. Brasseur, M. Charron, E. Manzini, M. A. Giorgetta, and T. Diehl (2006), The HAMMONIA Chemistry Climate Model: Sensititvity of the Mesopause Region to the 11-year Solar Cycle and CO_2 Doubling, *J. Clim.*, *19*(16), 3903–3931, doi:10.1175/JCLI3829.1.

Semenov, A. I. (2000), Long Term Temperature Trends for Different Seasons by Hydroxyl Emission, *Phys. Chem. Earth Part B*, *25*(5-6), 525–529.

Shapiro, A. V., E. Rozanov, A. I. Shapiro, S. Wang, T. Egorova, W. Schmutz, and T. Peter (2012), Signature of the 27-day solar rotation cycle in mesospheric OH and H_2O observed by the Aura Microwave Limb Sounder, *Atmos. Chem. Phys.*, *12*, 3181–3188, doi:10.5194/acp-12-3181-2012.

She, C. Y., and D. A. Krueger (2004), Impact of natural variability in the 11-year mesopause region temperature observation over Fort Collins, CO (41°N, 105°W), *Adv. Space Res.*, *34*, 330–336, doi:10.1016/j.asr.2003.02.047.

Sigernes, F., N. Shumilov, C. S. Deehr, K. P. Nielsen, T. Svenøe, and O. Havnes (2003), Hydroxyl rotational temperature record from the auroral station in Adventdalen, Svalbard (78°N, 15°E), *J. Geophys. Res.*, *108*(A9), 1342, doi:10.1029/2001JA009023.

Sigernes, F., J. M. Holmes, M. Dyrland, D. A. Lorentzen, S. A. Chernouss, T. Svenøe, J. Moen, and C. S. Deehr (2007), Absolute calibration of optical devices with a small field of view, *J. Opt. Technol.*, *74*(10), 669–674, doi:10.1364/JOT.74.000669.

Sigernes, F., et al. (2012), Hyperspectral all-sky imaging of auroras, *Opt. Express*, *20*(25), 27,650–27,660.

Sivjee, G. G., and R. M. Hamwey (1987), Temperature and chemistry of the polar mesopause OH, *J. Geophys. Res.*, *92*(A5), 4663–4672, doi:10.1029/JA092iA05p04663.

von Savigny, C., I. C. McDade, K.-U. Eichmann, and J. P. Burrows (2012), On the dependence of the OH^* Meinel emission altitude on vibrational level: SCIAMACHY observations and model simulations, *Atmos. Chem. Phys.*, *12*, 8813–8828, doi:10.5194/acp-12-8813-2012.

Winick, J. R., P. P. Wintersteiner, R. H. Picard, D. Esplin, M. G. Mlynczak, J. M. Russell III, and L. L. Gordley (2009), OH layer characteristics during unusual boreal winters of 2004 and 2006, *J. Geophys. Res.*, *114*, A02303, doi:10.1029/2008JA013688.

Wynn, T. A., and V. B. Wickwar (2009), The effects of model misspecification on linear regression coefficients as applicable to solar and linear terms, *Annual Report of the Rocky Mountain NASA Space Grant Consortium*.